



Effect of initial microstructure on microstructure evolution and mechanical properties of 0.12C martensitic steels during quenching and tempering

Ya-ru Wang^{1,2,3} · Zi-yong Hou³ · He Yang³ · Jun Zhao³ · Zhi-yuan Chang^{1,4} · Fan-mao Meng⁵ · Ling Zhang³ · Gui-lin Wu⁶ · Xiao-xu Huang³

Received: 9 November 2023 / Revised: 9 January 2024 / Accepted: 26 January 2024

© China Iron and Steel Research Institute Group Co., Ltd. 2024

Abstract

The microstructure evolution and mechanical properties of a Fe–0.12C–0.2Si–1.6Mn–0.3Cr–0.0025B (wt.%) steel with different initial microstructures, i.e., hot rolled (HR) and cold rolled–annealed (CRA), were studied through optical microscopy, scanning electron microscopy, electron channeling contrast imaging, microhardness and room temperature uniaxial tensile tests. After water quenching from 930 °C to room temperature, a fully martensitic microstructure was obtained in both as-quenched HR and CRA specimens, which shows a microhardness of 480 ± 5 HV, and no significant difference in microstructure and microhardness was observed. Tensile test results show that the product of tensile strength and total elongation (UTS \times TE) of the as-quenched HR specimen, i.e., 24.1 GPa%, is higher than that of the as-quenched CRA specimen, i.e., 18.9 GPa%. While, after being tempered at 300 °C, the martensitic microstructures and mechanical properties of the two as-quenched specimens change significantly due to the synergy role of the matrix phase softening and the precipitation strengthening. Concerning the maximum UTS \times TE, it is 18.9 GPa% obtained in the as-quenched CRA one, while that is 24.4 GPa% obtained in the HR specimen after tempered at 300 °C for 5 min.

Keywords Initial microstructure · Lath martensite · Quenching · Tempering · Mechanical property

✉ Zi-yong Hou
houzy@cqu.edu.cn

✉ Zhi-yuan Chang
changzyhpu@163.com

¹ State Key Laboratory of Vanadium and Titanium Resource Comprehensive Utilization, Panzhihua 617000, Sichuan, China

² State Key Laboratory of Advanced Special Steel, Shanghai Key Laboratory of Advanced Ferrometallurgy, School of Materials Science and Engineering, Shanghai University, Shanghai 200444, China

³ International Joint Laboratory for Light Alloys (Ministry of Education), College of Materials Science and Engineering, Chongqing University, Chongqing 400044, China

⁴ Institute of Steel Technology for Automobile and Household Appliance, Pangang Group Co., Ltd., Panzhihua 617000, Sichuan, China

⁵ ATB Motor (Shanghai) Co., Ltd., Keen International Center, Shanghai 200041, China

⁶ Beijing Advanced Innovation Center for Materials Genome Engineering, University of Science and Technology Beijing, Beijing 100083, China

1 Introduction

The worldwide movement toward carbon neutrality encourages the automobile industry to develop lightweight and ultra-/high-strength materials [1–4]. Steel is one of the most vital components for automobiles due to its good combination of affordability, exceptional machinability, and recyclability. Thus, the application of ultra-/high-strength steels in car bodies becomes a potential solution for lightweight and crashworthiness [4–8].

It is well known that two types of forming methods, i.e., cold stamping and hot stamping, have been widely applied for car body production. For the cold stamping process, even though it has been widely employed for forming high-strength steel sheets, there are several drawbacks, such as large springback, high load, low formability, short service life of tools, and severe wear [9]. To overcome these drawbacks, the hot stamping process, consisting of heating steel blank to a temperature above the finish temperature of austenization, holding it for 3–10 min, and then

transferring the steel sheet from the furnace to the hot stamping mould for simultaneous forming and quenching [10], has been developed. For example, the tensile strength of 22MnB5 steel, after subjected to hot-rolling, cold-rolling, and annealing, showing a ferritic–pearlitic microstructure, is approximately 600 MPa, while the tensile strength can reach 1600 MPa after hot stamping [11]. The tensile strength together with the absorbed energy of the hot stamping component was significantly enhanced. The hot stamping process was first applied to the impact-resistant side members of the Swedish SAAB 9000 model in the 1980s [12]. However, till now, the produced components by the hot stamping process take only 15%–38% of the total amount of components in body-in-white [13] due to the strength–ductility trade-off in steels.

It is a historical issue to achieve a good combination of ultra-high strength and toughness in steel. Lath martensitic steel containing less than 0.35 wt.% carbon, in general, was widely used. In the past decades, considerable progress has been made in developing ultra-high strength steels in such a low-carbon martensite [7, 14–18]. A significant body of research on low-alloy high-strength steels has demonstrated that the final microstructure of steel plays a crucial role in determining its mechanical behavior. Meanwhile, the strength and toughness of steels can be tuned by adding trace elements, such as Nb, V, Ti, Mo, and W, to form dispersion of nano precipitates and refine prior austenite grains by pinning effect [15, 16, 19–22]. By adding Nb element, a 2000 MPa grade ultra-high strength steel with the product of tensile strength and total elongation ($UTS \times TE$) ~ 17.7 GPa% has been developed by Liang et al. [15]. Furthermore, the optimal processing parameters are also equally important. An Fe–Mn–Si–Nb alloyed steel with a $UTS \times TE$, i.e., ~ 31.4 GPa%, has been produced through a novel quenching–partitioning–tempering process [17].

The microstructure of martensitic steel, such as morphology, size, and type, is related to the processing parameters and chemical composition, which determine the mechanical properties. The role of the initial microstructure of low-carbon lath martensitic steel on the subsequent as-quenched and tempered microstructure and mechanical properties has yet to receive attention. Luo et al. [23] suggested that the substructure of martensite, including packet, block, and lath, was refined when the size of prior austenite grains was decreased. Zhang et al. [24] found that adding Nb into 42CrNiMoV bolt steel can significantly refine the size of prior austenite grain and the corresponding as-quenched martensitic microstructure. Järvinen et al. [25] suggested that the austenitization parameters and the initial microstructure of 22MnB5 steel influence the grain size and morphology of austenite and its mechanical properties. Mirzadeh et al. [26] produced ferritic–

Table 1 Chemical composition of studied steel (wt.%)

C	Si	Mn	Cr	B	Fe
0.12	0.2	1.6	0.3	0.0025	Balance

martensitic dual-phase microstructures with different sizes, morphology, and distribution of martensite by altering the initial microstructures using heat treatment and thermo-mechanical processing routes. Yan et al. [27] found that initial microstructure has an impact on both microstructural evolution and mechanical properties. Detailed information concerning the effect of initial microstructure on the as-quenched and tempered microstructures and mechanical properties of low-carbon lath martensitic steels still needs to be included.

Therefore, the purpose of present study is to investigate the effect of initial microstructure on the microstructure evolution and the mechanical properties of low-carbon steel. The as-quenched and tempered microstructure and mechanical properties of 0.12C (wt.%) steel with different initial microstructures were studied by using a combination of optical microscopy, scanning electron microscopy (SEM), electron channeling contrast imaging (ECCI), microhardness and room temperature uniaxial tensile tests. The role of initial microstructure on the microstructure evolution and mechanical properties of lath martensitic steel was also further discussed.

2 Materials and methods

The chemical compositions of the studied steel are listed in Table 1. The alloy was made by vacuum induction melting and cast into an ingot. The forged ingot was cut into a 100 mm \times 100 mm \times L mm slab (L is the length of the ingot). Then, the slab was homogenized at 1250 °C for 2.5 h and hot-rolled to 3.5 mm in thickness (hereafter referred to as HR). The hot-rolled plate was then pickled and cold-rolled to 1.5 mm with a thickness reduction of 57.1%, after which it was annealed for 5 min at 750 °C (hereafter referred to as CRA).

The equilibrium phase fractions of the studied steel were calculated using the Thermo-Calc software with the TCFE12 database (see in Fig. 1) for a temperature range from 0 to 1400 °C, which was relevant for the solid phase observation. The start temperature of austenization (A_{c1}) and finish temperature of austenization (A_{c3}) are 684 and 823 °C, respectively, as seen in Fig. 1a. From the detailed magnification of Fig. 1a, austenite can completely transform into ferrite as the temperature drops below 684 °C. When the temperature continues to decrease, various types

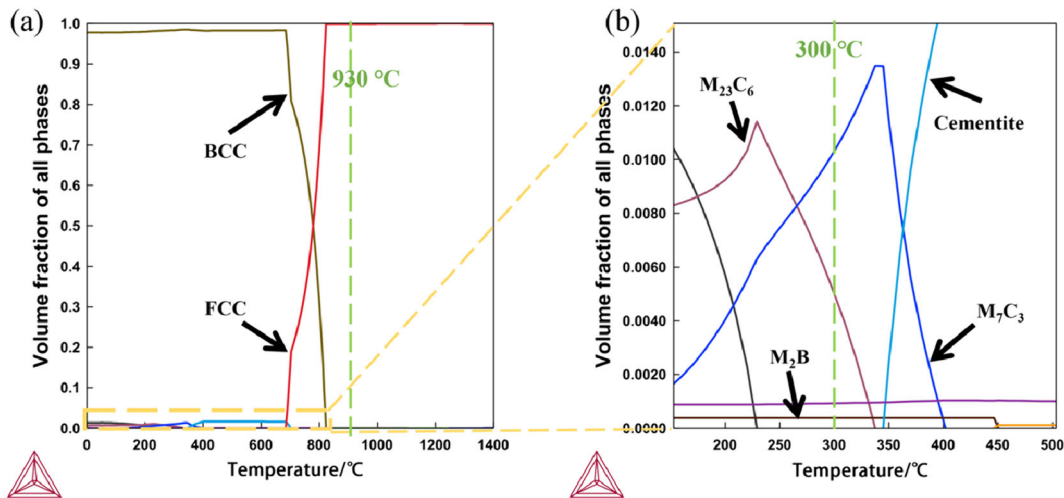


Fig. 1 Equilibrium phase diagram (a) and detailed magnification in a (b) of studied steel

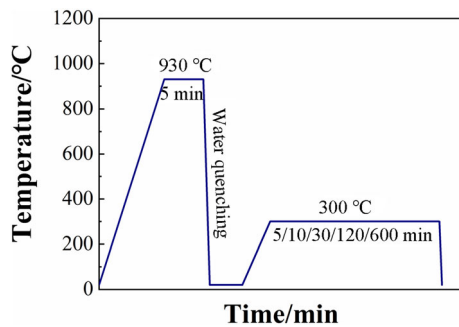


Fig. 2 Schematic of heat treatments used for each condition

of precipitates gradually form. When the temperature decreases to 447, 401 and 334 °C, the M_2B , M_7C_3 , and $M_{23}C_6$ carbides start to form, respectively. At 300 °C, the predominant precipitates are M_7C_3 (volume fraction of 1.06%), $M_{23}C_6$ (volume fraction of 0.48%), and M_2B (volume fraction of 0.04%).

Based on the calculated phase diagram, specimens with dimensions of 40 mm × 25 mm (rolling direction (RD) × transverse direction (TD)) were first cut from the HR and CRA plates by wire electrical discharge machining (Wire-EDM). The schematic of heat treatments is shown in Fig. 2. The specimens were austenitized at 930 °C for 5 min, followed by water quenching (hereafter referred to as HR-Q and CRA-Q, respectively). Then, the as-quenched specimens were tempered at 300 °C for 5, 10, 30, 120, and 600 min, respectively, which were hereafter referred to as HR/CRA-T 5, HR/CRA-T 10, HR/CRA-T 30, HR/CRA-T 120, and HR/CRA-T 600, respectively, for easy discussion. All the heat treatments were conducted using a GSL-1400X tube furnace.

The dog-bone tensile specimens were cut along with RD by Wire-EDM, as seen in Fig. 3. The tensile tests were

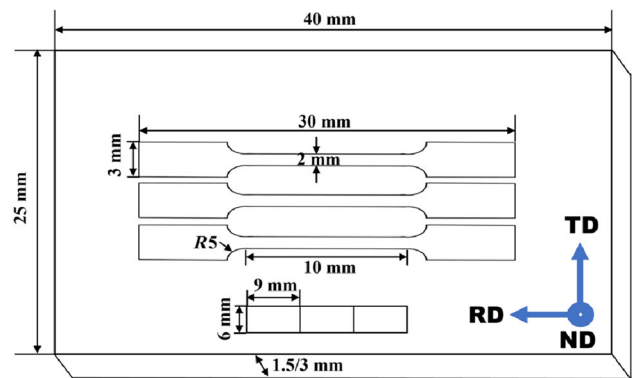


Fig. 3 Schematic illustration of tensile test specimens and metallographic specimens. ND—Normal direction

performed using SHIMADZU AG-X Plus (10 kN) with a specific crosshead speed of 0.5 mm/min, and three specimens were used for each condition.

The metallographic and microhardness test specimens were ground by SiC paper, mechanically polished with 0.5 μm diamond spray, and then etched in 4 vol.% Nital. The average grain size of ferrite and pearlite is calculated using an intercept method, and the nano measurer software is used. For each condition, ~ 500 grains were taken into account for an accurate statistical effect. The microstructure observations were carried out by MODEL DM2000X optical microscope and JEOL JSM-7800F field emission SEM, operating at 15 kV. The microhardness measurements were conducted under a constant loading condition using a load of 1.961 N for a dwell time of 15 s. An average value of 10 points for each specimen was taken, and the distance between neighboring indents was set longer than 150 μm to avoid interference.

3 Results

3.1 Thermodynamic calculations

Within the temperature range of 0–800 °C, the chemical composition in the matrix BCC, FCC, M_2B , M_7C_3 , and $M_{23}C_6$ is shown in Fig. 4a, b, c, d, respectively, indicating that the chemical composition in the matrix and precipitates changes to some extent with temperature. Notably, with the temperature decreasing, the Mn content of BCC and three types of precipitates, i.e., M_2B , M_7C_3 , and $M_{23}C_6$ increases first and then decreases, while the Mn content of FCC as a whole is on a downward trend. The content of Cr increases slowly in M_2B and increases significantly in $M_{23}C_6$. However, the change of Cr content in BCC and FCC is minor due to the low adding amount in total. Overall, the calculated results shown in Figs. 1 and 4 can guide heat treatments and alloy design and optimization, to minimize the addition of alloying elements and reach the expected phase and microstructure at the end.

3.2 Microstructure evolution during quenching and tempering

The initial microstructure is composed of polycrystal ferrite and pearlite in both HR and CRA specimens, as seen in Figs. 5a, b and 6a, b. The different features in microstructure between the HR and CRA specimens are the size, morphology, and distribution of ferrite and pearlite. It is clear that, in the HR specimen, the elongated pearlite and ferrite, along the hot rolling direction, are observed. A typical full recrystallization microstructure, instead of a deformed microstructure, of the CRA specimen is observed. The cold rolling and annealing are the main reason for such microstructure in the CRA specimen. In addition, the average grain size of ferrite in the CRA specimen, i.e., $7.5 \pm 2.1 \mu\text{m}$, is much smaller than that of the HR specimen, i.e., $10.5 \pm 4.2 \mu\text{m}$.

Figures 5c, d and 6c, d depict the as-quenched microstructure of HR and CRA specimens. Both specimens show a full lath martensitic microstructure. While, the fine and complicated martensitic microstructure, including prior austenite grain (PAG), packet, block, and lath, is somehow

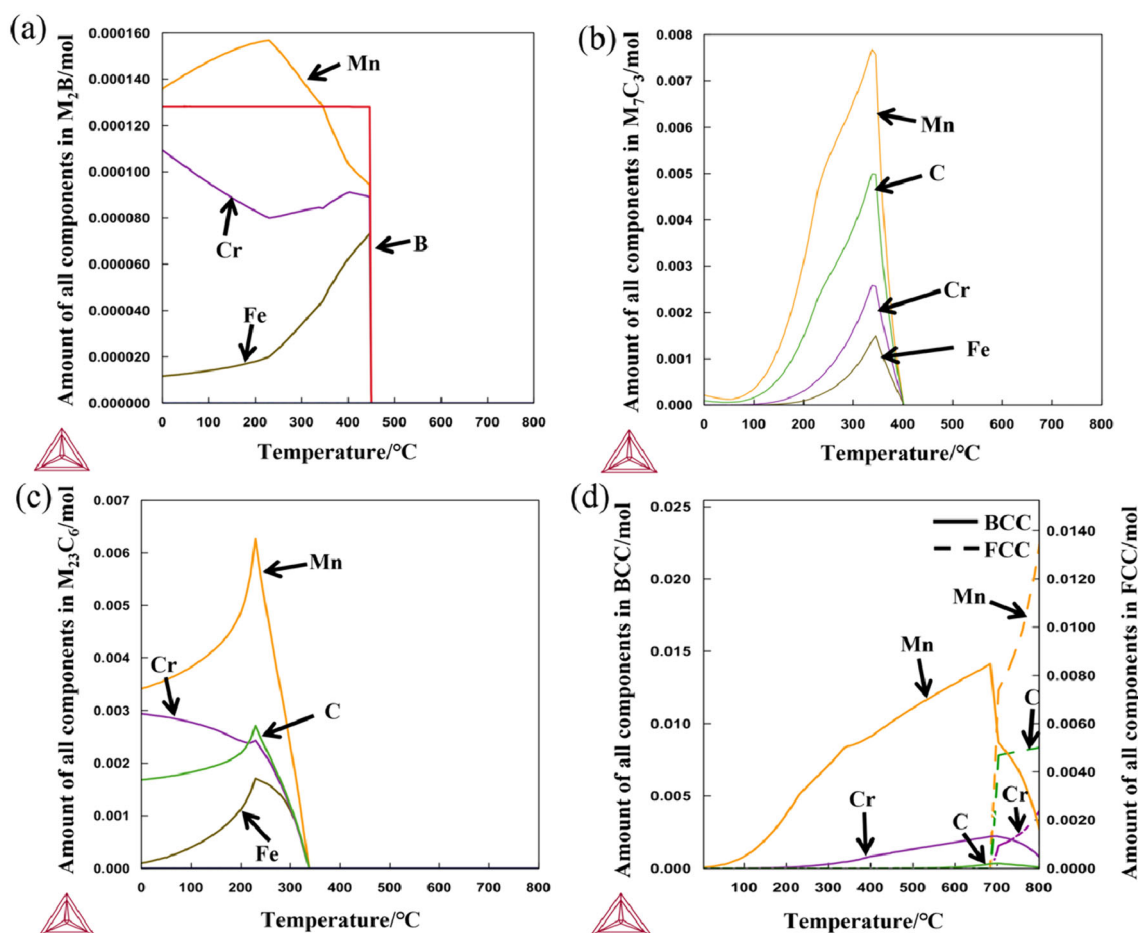


Fig. 4 Variation of chemical composition in M_2B (a), M_7C_3 (b), $M_{23}C_6$ carbides (c) and BCC and FCC with temperature (d)

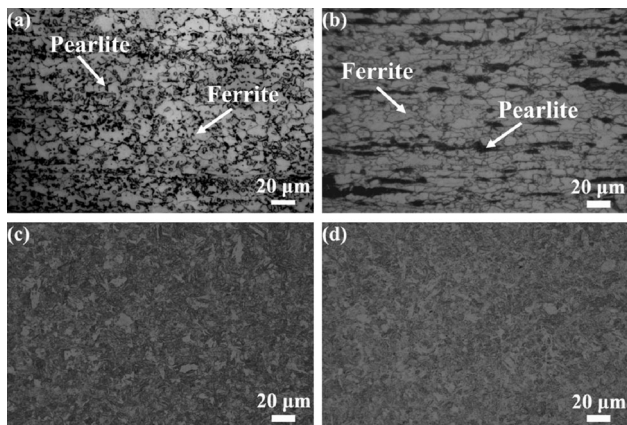


Fig. 5 OM microstructures of specimens. **a** CRA; **b** HR; **c** CRA-Q; **d** HR-Q

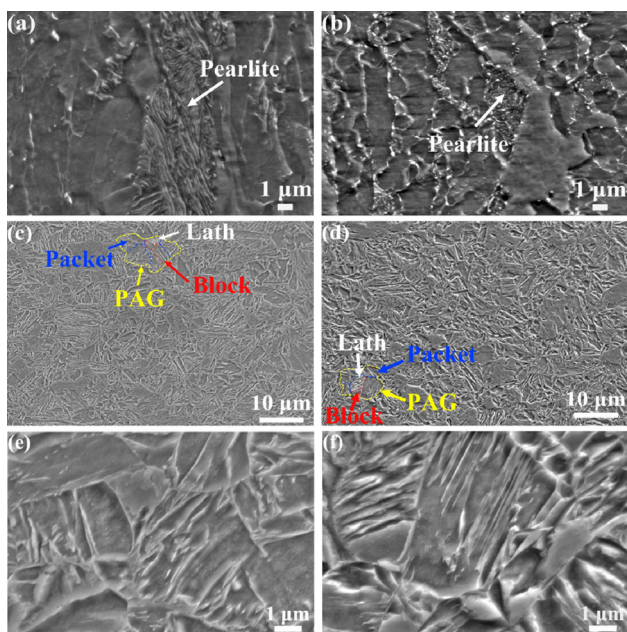


Fig. 6 SEM microstructures of specimens. **a** CRA; **b** HR; **c**, **e** CRA-Q; **d**, **f** HR-Q

clearly presented as shown in Fig. 6c, d, e.g., packet consists of several well-developed parallel blocks [28], even though the quantification for each type of substructure is a challenge so far. Compared with the as-quenched microstructure, the width of the lath in the HR specimen is slightly coarser than that in the CRA one. This could be because the growth of martensite is hindered in the CRA specimen by relatively dense boundaries, which are inherited from the initial condition. Interestingly, some fine carbides are distributed inside the coarse laths, while carbides are rarely observed inside the thin laths, as seen in Fig. 6e, f. Hutchinson et al. [29] pointed out that the martensite starting temperature (M_s) and the martensite finishing temperature (M_f) of 0.12C (wt.%) mild steels are

448 and 288 °C, respectively. Thus, during quenching to room temperature, carbon could diffuse to a distance from a few nanometers to tens of nanometers, depending on the quenching rate above M_s [30]. This phenomenon is called auto-tempering. For the present steel, the M_s and M_f are 423 and 314 °C, respectively, and the auto-tempering will also occur. A similar phenomenon has been reported by Morsdorf et al. [31] and Cai et al. [32] in other types of steels.

The microstructures of the tempered CRA and HR specimens are shown in Figs. 7 and 8, respectively. No significant change occurs after tempering for 5 min in both steels. When the tempering time is prolonged to 10 min, the precipitates can be found inside the thin laths, other than in the coarse laths only. After tempering for 120 and 600 min, the volume fraction and the size of the precipitates are increased. Meanwhile, the coarsening of thin lath also occurs due to the migration and elimination of low-angle lath boundaries, as seen in Figs. 7 and 8. Furthermore, with increasing tempering time [33] or temperature [34], the sizes of inter-lath carbides increase noticeably due

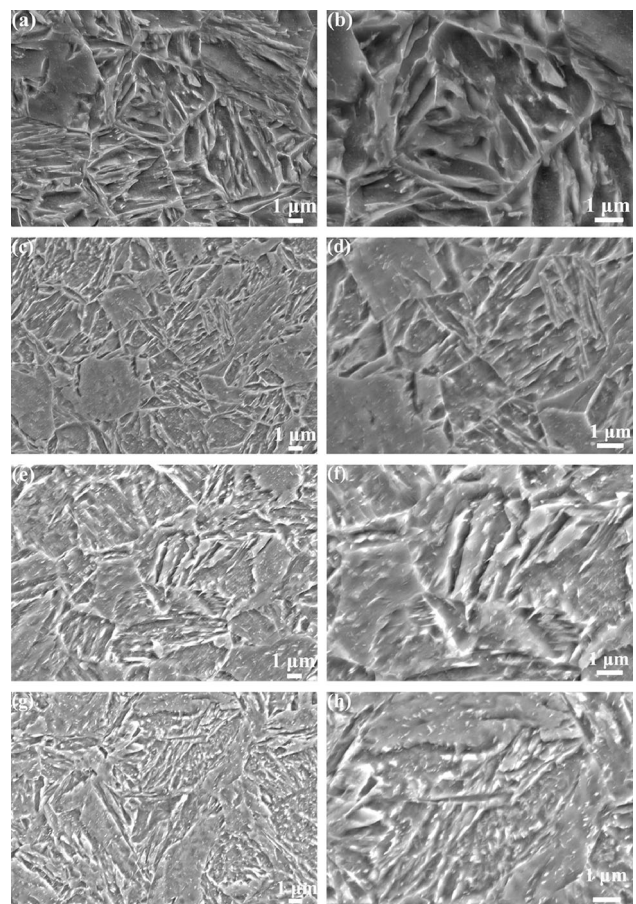


Fig. 7 SEM microstructure of CRA specimen tempered at 300 °C. **a**, **b** CRA-T 5; **c**, **d** CRA-T 10; **e**, **f** CRA-T 120; **g**, **h** CRA-T 600

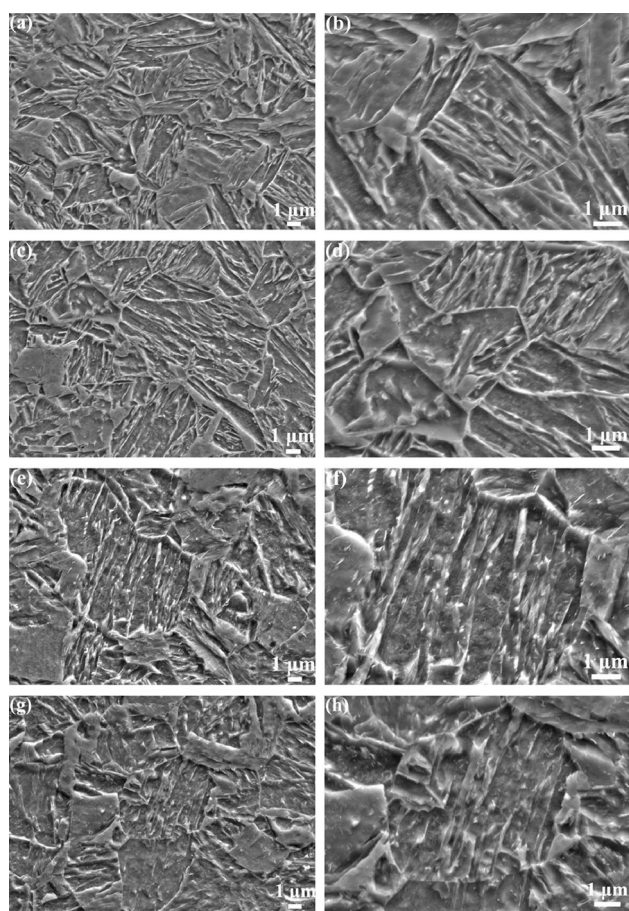


Fig. 8 SEM microstructure of HR specimen tempered at 300 °C. **a**, **b** HR-T 5; **c**, **d** HR-T 10; **e**, **f** HR-T 120; **g**, **h** HR-T 600

to the faster grain boundary diffusion. In contrast, the sizes of intra-lath carbides remain nearly constant.

To further understand the as-quenched and tempered microstructure, typical ECCIs are also given in Fig. 9. The lath boundaries are straight in the as-quenched specimen. Two types of laths, i.e., thin (~ 80 nm) and coarse (~ 640 nm), are found, which is similar to the earlier reports in Fe–C–Cr alloys by Hou et al. [35, 36]. After tempering for 5 min, the lath boundaries become curved instead of straight all the way, as seen in Fig. 9b. After tempering for 600 min, a large number of circular precipitates are coarsened to a size of 34 ± 6 nm in diameter, and a few elongated precipitates are also observed (seen in Fig. 9c). The width of laths also coarsens from 209 ± 43 to 788 ± 103 nm.

3.3 Mechanical properties

After quenching, the microhardness of the two specimens is 480 ± 5 HV, which mainly depends on the carbon content in a specific range, e.g., < 0.65 wt.% [36]. Normally, the dislocation density of the as-quenched

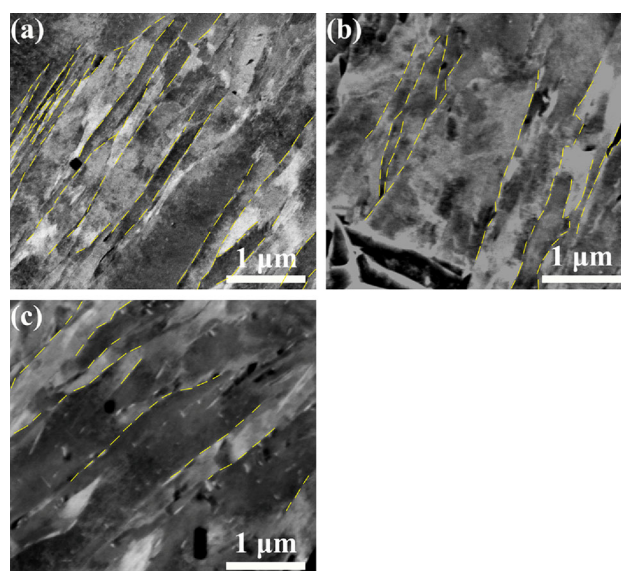


Fig. 9 ECCI microstructure of CRA specimens. **a** CRA-Q; **b** CRA-T 5; **c** CRA-T 600

martensite is in the range of 10^{15} to 10^{16} m^{-2} , which mainly depends on the carbon content [37] as well as weakly related with other factors, e.g., alloying elements. A large number of studies have been conducted on the changes in dislocation density during tempering at different temperatures and time [35–41]. A similar trend in dislocation evolution, i.e., decreases sharply in the first few seconds and goes down slightly afterward, and then keeps almost constant at the end, is always observed, no matter how the chemical composition varies [35–39]. Therefore, here we did not present the conventional X-ray diffraction (XRD) measurements to estimate the dislocation density, even though it could provide an approximate value and strongly depends on the data process and equipment settings. Meanwhile, the supersaturated carbon atoms escape from the matrix, and various defects form carbides, leading to the relaxation of lattice distortion and reduction of solid solution strengthening [37, 38]. These microstructural changes would contribute to the variation of mechanical properties, including strength and ductility, referred to as microhardness, as seen in Fig. 10. Notably, there is a small increment in the HR-Q specimen after tempering for time longer than 10 min, which could be related to the precipitation strengthening caused by a considerable number of fine precipitates formed during tempering [21, 40, 41]. With the prolonged tempering time, the microhardness for both types of specimens, i.e., CRA-T 600 and HR-T 600, are almost constant. The lath martensite is stabilized during the tempering due to the strong pinning effect of fine precipitates [33, 35, 42, 43] and the low driving force of boundary migration at such low temperatures, i.e., 300 °C [37].

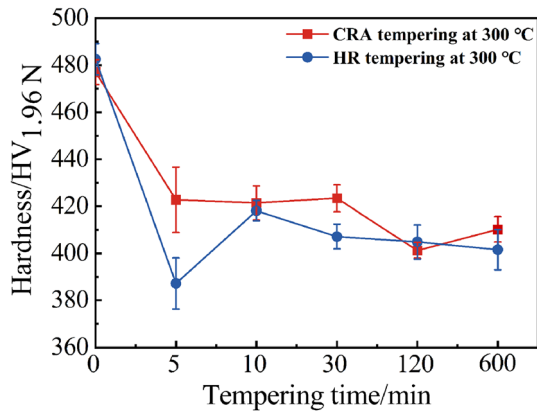


Fig. 10 Microhardness of as-quenched and tempered HR and CRA specimens

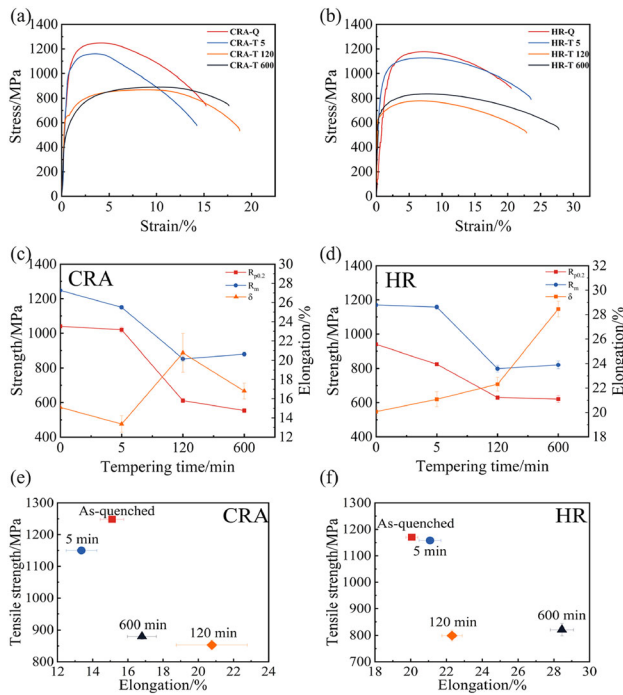


Fig. 11 Tensile properties of CRA and HR steels under different conditions. **a, b** Stress–strain curve; **c, d** ultimate tensile strength, yield strength, and elongation; **e, f** UTS \times TE

The mechanical properties of the HR and CRA specimens after tempering for different time are shown in Fig. 11. The tensile properties with the tempering time shown in Fig. 11a, d are consistent with the microhardness with the tempering time shown in Fig. 10. According to Fig. 11e, f and Table 2 (listing the UTS \times TE), the maximum UTS (1248 ± 1 MPa) \times TE ($15.1\% \pm 0.7\%$), i.e., 18.9 GPa% is obtained in the as-quenched state for CRA specimen, while in the HR specimen, the maximum UTS

Table 2 UTS \times TE of CRA and HR specimens under different conditions

Specimen	UTS \times TE/GPa%
CRA-Q	18.9 ± 0.85
CRA-T 5	15.3 ± 1.13
CRA-T 120	16.3 ± 2.03
CRA-T 600	15.7 ± 0.90
HR-Q	24.1 ± 0.59
HR-T 5	24.4 ± 0.98
HR-T 120	17.7 ± 0.90
HR-T 600	23.2 ± 1.19

(1158 ± 13 MPa) \times TE ($21.08\% \pm 0.6\%$), i.e., 24.4 GPa%, is obtained after 5 min of tempering. After tempering for 120 min, the UTS \times TE of the CRA specimen are 853 ± 15 MPa and $20.77\% \pm 2.0\%$, respectively, while the tensile strength of the HR specimen reached 799 ± 20 MPa at 120 min of tempering, and the elongation of the HR specimen reached a maximum value of $28.45\% \pm 0.6\%$ at tempering for 600 min.

4 Discussion

4.1 Effect of initial microstructure on quenching and tempering microstructure

No matter with the CRA and HR specimens, polycrystalline ferrite and blocky pearlite are the initial microstructure. The only main difference between the CRA and HR specimens is the morphology and size of the ferrite grain, as seen in Fig. 5a, b and Fig. 6a, b. This is mainly because a significant recovery and even recrystallization occur during the hot rolling at elevated temperatures [40, 44]. The CRA specimen shows a typical full recrystallization microstructure, instead of a deformed feature, which is observed due to cold rolling and annealing, while in the HR specimen, the elongated pearlite and ferrite along the hot rolling direction are obtained.

After water quenching, the width of the lath in the HR-Q specimen is coarser than that in the CRA-Q, as seen in Fig. 6c, d. The finer the initial microstructure in the steel, the finer the austenite grains and thus the as-quenched martensitic microstructure [23, 24, 45–47]. Thus, it is concluded that the initial austenite grains can refine the substructure of martensite, such as block and lath [48, 49]. The M_s temperature in the steels, i.e., below 0.1–0.2 wt.% C, is always higher than the room temperature, and the carbon can partition carbon from the super-saturated fresh martensite to various defects, such as dislocation, to form carbides after quenched below the M_s temperature [50, 51].

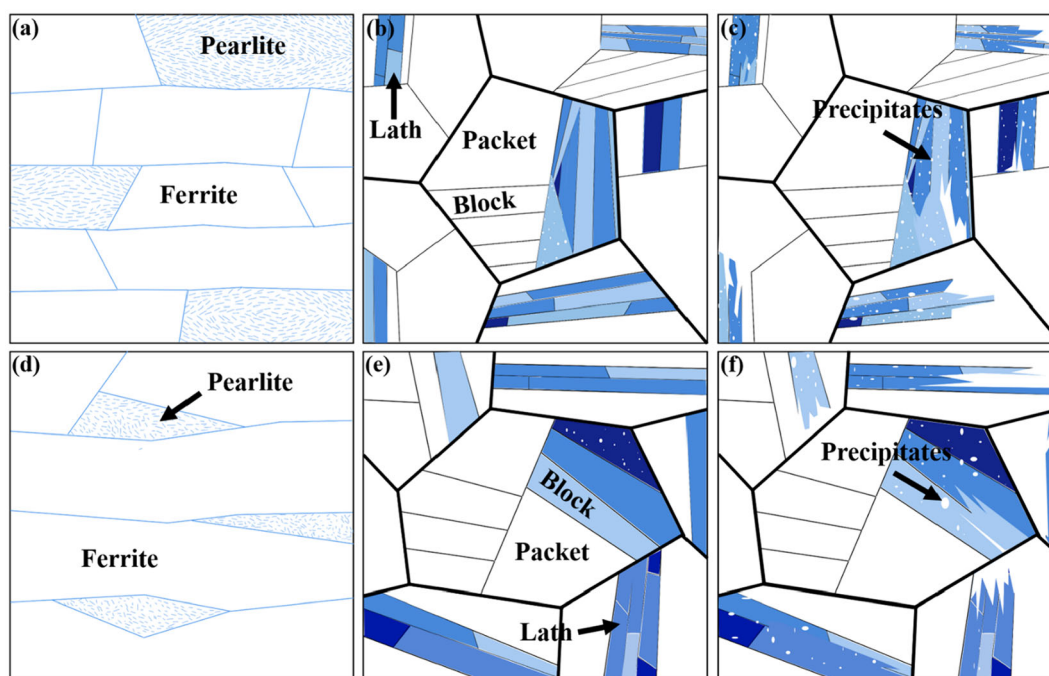


Fig. 12 Schematic of microstructure evolution in studied steels during quenching and tempering of CRA (a–c) and HR (d–f). **a, d** Initial microstructure (ferrite and pearlite); **b, e** as-quenched

microstructure (fresh martensite, thicker black lines represent prior austenite grains); **c, f** tempered martensite obtained by long-term tempering

During the auto-tempering, the width of primarily formed laths becomes coarse due to boundary migration and merging. The diffusion distance of carbon is also longer than the lath formed at the late stage, which is always regarded as the more prone auto-tempering area, as shown in Fig. 6e, f.

After being tempered for a short time, the as-quenched martensite has very high density dislocations, which provides plenty of potential nucleation sites for the precipitate [49]. Then, a large number of dispersed precipitates are rapidly formed at intra/inter laths. With the extension of the tempering time, the size of the precipitates gradually grows, which leads to the weakening of the pinning effect of the precipitates, and the laths are also coarse [52]. The difference in the initial microstructure of CRA and HR specimens would inhabit the as-quenched microstructure, leading to microstructure differences, e.g., the density of dislocation and solid solution of elements in the matrix phase. Then, during the tempering, the microstructure evolution of martensite, including migration of various grain boundaries, nucleation, and growth of precipitates, are strongly related to the as-quenched one, which is the main reason for the microstructure difference in the CRA and HR specimens. The schematic of microstructure evolution during the heating treatment is summarized in Fig. 12. In the final tempered microstructure, the volume fraction of the precipitates in the CRA specimen is larger, and precipitates are evenly dispersed across the matrix, while the precipitates in the HR specimen appear to be primarily at lath boundaries, and the

obtained laths are coarser. Quantity studies have shown that the finer the initial grain size, the more potential nucleation sites of the precipitate phase, and therefore the higher the volume fraction of the precipitates forms in a short time [53]. From SEM taken in randomly selected areas (Figs. 7 and 8 represent that of the CRA and the HR specimens, respectively), it can be seen that the precipitates in the CRA specimens occupy a larger volume fraction.

4.2 Effect of initial microstructure on mechanical properties

After quenching, full lath martensite is observed in both CRA and HR specimens, showing a microhardness of 480 ± 5 HV. This is consistent with the earlier report on steels with similar carbon content [36] and mainly depends on the carbon content rather than other alloying elements. After tempering at $300\text{ }^{\circ}\text{C}$ for various time, the microhardness changing trend in these two specimens is roughly the same. The microhardness decreases abruptly in the first 5 min tempering and then keeps constant within a specific range, i.e., from 480 ± 5 HV to 410 ± 5 HV (CRA) and 401 ± 8 HV (HR) as tempering time changes from 10 to 600 min. During the first 5 min tempering, the lattice distortion is released, and the dislocation density is significantly decreased due to the recovery of as-quenched martensite [37, 53]. Thus, the microhardness and tensile strength of the two specimens rapidly reduced for both the

CRA and HR specimens. After tempering for 30 min, the microhardness of the CRA specimen is almost unchanged due to the synergy precipitation strengthening and matrix softening. At the same time, the microhardness of the HR specimen is slightly increased. With the prolonged tempering time, the matrix softening and precipitation strengthening reach an equilibrium condition, leading to a stable microhardness for both specimens. It should be noticed that the tensile strength of both types of specimens decreases with the tempering time prolonging.

Unlike the microhardness, the tensile strength and total elongation of CRA-Q specimens are slightly higher and lower than those of the HR-Q specimen, respectively. This may be caused by the combined effect of grain boundary strengthening [40] due to the fine substructure in the CRA specimen. When tempering at 300 °C for various time, the softening of the matrix leads to a decrease in the microhardness, especially at the very early stage, owing to the rapid release of internal stress and annihilation of high mobility of dislocation [37]. This leads to a decrease in the tensile strength and an increase in the total elongation. Meanwhile, the supersaturated alloying elements will diffuse to the place with carbon segregation or defects to form carbides. The Ashby-Orowan model is adapted for cubic polycrystalline materials with spherical precipitates and is used to evaluate the precipitation strengthening,

$$\Delta\sigma_{\text{ppt}} = \left(\frac{0.538Gb f^{\frac{1}{2}}}{X} \right) \ln \left(\frac{X}{2b} \right) \quad (1)$$

where $\Delta\sigma_{\text{ppt}}$ is the amount of precipitation strengthening; G is the shear modulus, with a value of 8.3×10^4 MPa; b is the magnitude of the Burgers vector taken by 0.248 nm; f is the volume fraction of the precipitates; and X is the diameter of the precipitates expressed in nm [54]. According to the equilibrium phase diagram as shown in Fig. 1, the volume fractions of M_2B , M_7C_3 and $M_{23}C_6$ precipitates at 300 °C are 0.04%, 1.06% and 0.48%, respectively. Thus, we assume that the volume fractions are 0.79% (half of the equilibrium value) at the initial stage and 1.58% after tempering at 300 °C for 600 min, respectively. We assume that the initial size of precipitates is 1 nm (at the very early stage of nucleation and growth, i.e., as-quenched condition), while that is about 34 nm after tempered at 300 °C for 600 min according to the microstructure observation. Thus, the strengthening contribution by the precipitates varies in the range of 173–690 MPa, as shown in Table 3. Therefore, with tempering time prolonging, the size of precipitates gets coarser, as seen in Fig. 9, and the precipitation-strengthening effect weakens [37]. When tempering for 5 min, the tensile strength of the two specimens decreases, i.e., from 1248 ± 1 to 1159 ± 28 MPa (CRA) and from 1176 ± 21

Table 3 Precipitation contributions as a function of tempering time

Tempering time/min	Diameter/nm	Shear modulus/MPa	Burgers vector/nm	Precipitation strengthening/MPa
0	1	8.3×10^4	0.248	173
600	34	8.3×10^4	0.248	690

to 1158 ± 13 MPa (HR). When the tempering time is prolonged to 120 min or even 600 min, the tensile strength of CRA specimen decreases by 368–395 MPa, and the elongation increases by 1.7%–5.7%. Meanwhile, the tensile strength of HR specimen decreased by 349–370 MPa, and the elongation increased by 2.3%–8.4%. The findings pave the way for high-performance steel design by optimizing the initial microstructure before quenching and tempering.

5 Conclusions

1. The microstructure of as-quenched CRA and HR specimens is fully martensite, showing a microhardness of 480 ± 5 HV for both specimens, no matter the morphology and grain size of the initial microstructure. The different features in microstructure between the HR and CRA specimens are the size, morphology, and distribution of ferrite and pearlite, leading to a difference in the as-quenched microstructure.
2. After tempering at 300 °C for different time, a competitive process of precipitation strengthening and matrix phase softening occurs. At 5 min tempering, the microhardness of the HR and CRA specimens decreased rapidly due to the matrix softening during the very early stage of the fast recovery, and at 10 min tempering, a large number of precipitates were nucleated at inter/intra laths. The microhardness of the CRA specimen remained stable, while the microhardness of the HR specimen increased slightly. At 120 min tempering, the microhardness of the two specimens remained stable.
3. The mechanical properties of the studied steel can be tuned in an extensive range via initial microstructure control together with tempering parameters. The maximum UTS \times TE, i.e., 18.9 GPa%, of the CRA specimen, is obtained in the as-quenched specimen. In contrast, for the HR specimen, that is 24.4 GPa% after being tempered at 300 °C for 5 min.

Acknowledgements This research was funded by the Chongqing Natural Science Foundation (No. CSTB2022NSCQ-MSX1394), Graduate Research and Innovation Foundation of Chongqing, China (Grant No. CYS22008), Open Project of State Key Laboratory of Advanced Special Steel, Shanghai Key Laboratory of Advanced Ferrometallurgy, Shanghai University (SKLASS 2023-10) and the

Science and Technology Commission of Shanghai Municipality (No. 19DZ2270200), and the Open Project of the Large Casting and Forging Manufacturing Technology Engineering Center of Shanghai Institute of Mechanical and Electrical Engineering, State Key Laboratory of Vanadium and Titanium Resources Open Fund (No. 2022P4FZG04A).

Declarations

Conflicts of interest Zi-yong Hou is a youth editorial board member for *Journal of Iron and Steel Research International* and was not involved in the editorial review or the decision to publish this article. The authors declare no conflict of interest.

References

- [1] E. Scharifi, T. Schade, A. Ademaj, S.V. Sajadifar, U. Weidig, T. Niendorf, K. Steinhoff, *Steel Res. Int.* 92 (2021) 2000633.
- [2] H.X. Yin, Z.Z. Zhao, A.M. Zhao, X. Li, H.J. Hu, J.T. Liang, *J. Iron Steel Res. Int.* 22 (2015) 622–629.
- [3] W. He, B.L. Wang, Y. Yang, Y.H. Zhang, L. Duan, Z.P. Luo, C.J. Song, Q.J. Zhai, *J. Iron Steel Res. Int.* 25 (2018) 830–838.
- [4] M. Tisza, I. Czinege, *Int. J. Light. Mater. Manuf.* 1 (2018) 229–238.
- [5] H. Karbasian, A.E. Tekkaya, *J. Mater. Process. Technol.* 210 (2010) 2103–2118.
- [6] C.P. Couto, R.I. Revilla, R. Politano, I. Costa, Z. Panossian, I. De Graeve, J.L. Rossi, H. Terryn, *Corros. Sci.* 190 (2021) 109673.
- [7] W. Huang, H. Gu, Q. Liu, T. Si, *Mater. Chem. Phys.* 256 (2020) 123729.
- [8] Y.X. Qiao, Z.B. Zheng, H.K. Yang, J. Long, P.X. Han, *J. Iron Steel Res. Int.* 30 (2023) 1463–1476.
- [9] K. Mori, P.F. Bariani, B.A. Behrens, A. Brosius, S. Bruschi, T. Maeno, M. Merklein, J. Yanagimoto, *CIRP Ann.* 66 (2017) 755–777.
- [10] S.S. Li, H.W. Luo, *Int. J. Miner. Metall. Mater.* 28 (2021) 741–753.
- [11] H. So, D. Faßmann, H. Hoffmann, R. Golle, M. Schaper, *J. Mater. Process. Technol.* 212 (2012) 437–449.
- [12] T. Taylor, A. Clough, *Mater. Sci. Technol.* 34 (2018) 809–861.
- [13] I. Wróbel, A. Skowronek, A. Grajcar, *Symmetry* 14 (2022) 969.
- [14] B. Hu, H. Luo, F. Yang, H. Dong, *J. Mater. Sci. Technol.* 33 (2017) 1457–1464.
- [15] J. Liang, H. Lu, L. Zhang, F. Li, R. Cao, K. Liu, H. Pan, H. Teng, X. Li, A. Guo, Z. Zhao, *Mater. Sci. Eng. A* 801 (2021) 140419.
- [16] Y.T. Lin, H.L. Yi, Z.Y. Chang, H.C. Lin, H.W. Yen, *Front. Mater.* 7 (2020) 611390.
- [17] K. Zhang, P. Liu, W. Li, Z. Guo, Y. Rong, *Mater. Sci. Eng. A* 619 (2014) 205–211.
- [18] Y.J. Li, G. Yuan, L.L. Li, J. Kang, F.K. Yan, P.J. Du, D. Raabe, G.D. Wang, *Science* 379 (2023) 168–173.
- [19] J.B. Dong, K. Li, L.X. Gao, C.S. Li, *Tungsten* 5 (2023) 512–521.
- [20] Y. Zhang, C. Zhao, M. Sato, G. Miyamoto, T. Furuhashi, *ISIJ Int.* 61 (2021) 1641–1649.
- [21] Y. Tian, H. Yu, T. Zhou, K. Wang, Z. Zhu, *Mater. Character.* 188 (2022) 111919.
- [22] Z.B. Liu, Z. Yang, J.X. Liang, Z.Y. Yang, G.M. Sheng, *J. Iron Steel Res. Int.* 29 (2022) 207–214.
- [23] H. Luo, X. Wang, Z. Liu, Z. Yang, *J. Mater. Sci. Technol.* 51 (2020) 130–136.
- [24] C. Zhang, W. Hui, X. Zhao, Y. Zhang, X. Zhao, *Eng. Fail. Anal.* 135 (2022) 106144.
- [25] H. Järvinen, M. Isakov, T. Nyysönen, M. Järvenpää, P. Peura, *Mater. Sci. Eng. A* 676 (2016) 109–120.
- [26] H. Mirzadeh, M. Alibeyki, M. Najafi, *Metall. Mater. Trans. A* 48 (2017) 4565–4573.
- [27] S. Yan, X. Liu, T. Liang, Y. Zhao, *Mater. Sci. Eng. A* 712 (2018) 332–340.
- [28] S. Morito, H. Tanaka, R. Konishi, T. Furuhashi, T. Maki, *Acta Mater.* 51 (2003) 1789–1799.
- [29] B. Hutchinson, J. Hagström, O. Karlsson, D. Lindell, M. Tornberg, F. Lindberg, M. Thuvander, *Acta Mater.* 59 (2011) 5845–5858.
- [30] L. Morsdorf, E. Emelina, B. Gault, M. Herbig, C.C. Tasan, *Acta Mater.* 205 (2021) 116521.
- [31] L. Morsdorf, C.C. Tasan, D. Ponge, D. Raabe, *Acta Mater.* 95 (2015) 366–377.
- [32] H.L. Cai, P. Chen, J.K. Oh, Y.R. Cho, D. Wu, H.L. Yi, *Scripta Mater.* 178 (2020) 77–81.
- [33] Z. Hou, R.P. Babu, P. Hedström, J. Odqvist, *Mater. Sci. Technol.* 36 (2020) 887–893.
- [34] Y.M. Zhu, Q. Zhang, Q. Yuan, J.S. Guan, Y.B. Yang, G. Xu, *Arab. J. Sci. Eng.* 47 (2022) 9061–9073.
- [35] Z.Y. Hou, R.P. Babu, P. Hedström, J. Odqvist, *J. Mater. Sci.* 53 (2018) 6939–6950.
- [36] Z. Hou, P. Hedström, Y. Xu, W. Di, J. Odqvist, *ISIJ Int.* 54 (2014) 2649–2656.
- [37] G. Krauss, *Steel Res. Int.* 88 (2017) 1700038.
- [38] F. Liu, K. Chen, C. Kang, Z. Jiang, S. Ding, *J. Mater. Res. Technol.* 19 (2022) 779–793.
- [39] W. Ding, T. Wu, L. Sun, C. Yan, X. Lu, X. Lei, *Steel Res. Int.* 93 (2022) 2100627.
- [40] A. Dutta, D. Ponge, S. Sandlöbes, D. Raabe, *Mater. Sci. Forum* 941 (2018) 198–205.
- [41] B. Dou, H. Zhang, Y. Tao, Q.S. Ma, S. Guo, *Tungsten* 5 (2023) 189–197.
- [42] A. Kostka, K. Tak, R. Hellmig, Y. Estrin, G. Eggeler, *Acta Mater.* 55 (2007) 539–550.
- [43] Y.H. Yu, Z.D. Liu, Z. Liu, Z.Z. Chen, H.S. Bao, C. Zhang, Z.G. Yang, *J. Iron Steel Res. Int.* 30 (2023) 1279–1290.
- [44] B. Hu, X. Tu, H. Luo, X. Mao, *J. Mater. Sci. Technol.* 47 (2020) 131–141.
- [45] X. Liu, K.Y. Zhao, Y.H. Zhou, D. Ye, W. Jiang, Q.L. Yong, J. Su, *Adv. Mater. Res.* 393–395 (2011) 440–443.
- [46] M.A. Shtremel', V.I. Lizunov, V.V. Shkatov, *Met. Sci. Heat Treat.* 21 (1979) 747–750.
- [47] N.T. Egorov, M.S. Podgaiskii, L.I. Razumova, *Met. Sci. Heat Treat.* 21 (1979) 861–865.
- [48] D. Ning, C.R. Dai, J.L. Wu, Y.D. Wang, Y.Q. Wang, Y. Jing, J. Sun, *Mater. Character.* 176 (2021) 111111.
- [49] M.S. Mohsenzadeh, *J. Mater. Eng. Perform.* 32 (2023) 164–169.
- [50] G. Badinier, C.W. Sinclair, X. Sauvage, X. Wang, V. Bylik, M. Gouné, F. Danoix, *Mater. Sci. Eng. A* 638 (2015) 329–339.
- [51] T. Kohne, J. Fahlkrans, A. Stormvinter, E. Maawad, A. Winkelmann, P. Hedström, A. Borgenstam, *Metall. Mater. Trans. A* 54 (2023) 1083–1100.
- [52] Z. Liu, Z. Liu, X. Wang, C. Dong, Z. Chen, H. Bao, *Mater. Res. Express* 6 (2019) 116527.
- [53] C.L. Miao, C.J. Shang, H.S. Zurob, G.D. Zhang, S.V. Subramanian, *Metall. Mater. Trans. A* 43 (2012) 665–676.
- [54] T. Gladman, *Mater. Sci. Technol.* 15 (1999) 30–36.

Springer Nature or its licensor (e.g. a society or other partner) holds exclusive rights to this article under a publishing agreement with the author(s) or other rightsholder(s); author self-archiving of the accepted manuscript version of this article is solely governed by the terms of such publishing agreement and applicable law.